




RESEARCH ARTICLE

An idealized numerical study of tropical cyclogenesis and evolution at the Equator

Gerard Kilroy¹  | Roger K. Smith¹  | Michael T. Montgomery² 

¹Meteorological Institute,
Ludwig-Maximilians University of
Munich, Munich, Germany

²Department of Meteorology, Naval
Postgraduate School, Monterey, California

Correspondence

G. Kilroy, Meteorological Institute,
Ludwig-Maximilians University of
Munich, Theresienstr. 37, 80333 Munich,
Germany.
Email: gerard.kilroy@lmu.de

Funding information

Deutsche Forschungsgemeinschaft, KO
2248/2-1; National Science Foundation,
AGS-1313948; Office of Naval Research,
N0001417WX00336

Abstract

Tropical cyclone formation and evolution at, or near, the Equator is explored using idealized three-dimensional model simulations, starting from a prescribed, initial, weak counterclockwise rotating vortex in an otherwise quiescent, *nonrotating* environment. Three simulations are carried out in which the maximum tangential wind speed (5 m s^{-1}) is specified at an initial radius of 50, 100, or 150 km. After a period of gestation lasting between 30 and 60 hr, the vortices intensify rapidly, the evolution being similar to that for vortices away from the Equator. In particular, the larger the initial vortex size, the longer the gestation period, the larger the maximum intensity attained, and the longer the vortex lifetime. Beyond a few days, the vortices decay as the cyclonic vorticity source provided by the initial vortex is depleted and negative vorticity surrounding the vortex core is drawn inwards by the convectively driven overturning circulation. In these negative vorticity regions, the flow is inertially/centrifugally unstable. The vortex evolution during the mature and decay phases differs from that in simulations away from the Equator, where inertially unstable regions are much more limited in area. Vortex decay in the simulations appears to be related intimately to the development of inertial instability, which is accompanied by an outward-propagating band of deep convection. The degree to which this band of deep convection is realistic is unknown.

KEYWORDS

tropical cyclogenesis, tropical depressions, tropical lows

1 | INTRODUCTION

The majority of tropical cyclones form at latitudes beyond 5° from the Equator, where it is assumed the Earth's background rotation is sufficient to support vortex spin-up (e.g., Anthes, 1982, p. 48; Gill, 1982, p. 476; Houze,

1993, p. 406; Pielke and Pielke, 1997, p. 82; Wallace and Hobbs, 2006, p. 369). However, in the current International Best Track for Climate Stewardship (IBTrACS) version 4 (v04r00) dataset (Knapp *et al.* 2010), 35 tropical storms are listed as forming between 3°N and 3°S during the period 1848–2019. During the same time period, 105 cyclones

are listed as forming within 4° of the Equator and 231 cyclones (or 1.74% of the total) are listed as forming within 5° of the Equator.¹ One noteworthy example is Typhoon *Vamei*, which was first classified as a tropical depression at about 1.5°N latitude on December 26, 2001 over the South China Sea. This storm made landfall two days later along the southeastern coastline of the Malaysian Peninsula at 1.6°N , about 50 km north of Singapore (Chang *et al.*, 2003; Chang and Wong, 2008).

Another noteworthy entry in the IBTrACS dataset is Typhoon *Agnes* (1984), which formed essentially on the Equator, at 0.1°N , 148.5°E . *Agnes* intensified as it tracked to the northwest, attaining a maximum wind speed of 52.5 m s^{-1} (189 km hr^{-1}) at a latitude of 11.2°N . It made landfall at near-peak intensity on Samar Island in the Philippines, and later reintensified over the South China Sea before making landfall for a second time over Vietnam. The impact of *Agnes* was catastrophic, with just over 1,000 confirmed deaths and monetary damage of close to \$100 million (at 1984 values). Most of the loss of life and damage due to *Agnes* occurred in the Philippines.

Other examples of formation near the Equator are those of Typhoon *Sarah* (1956), which formed at 1.7°N (Fortner, 1958), and Typhoon *Kate* (1970), which formed and intensified into a major typhoon while located equatorward of 5°N (Holliday and Thompson, 1986). Typhoon *Kate* had a somewhat small inner core size, with an eye diameter of just 31 km observed on October 16, 1970. Typhoon *Vamei* showed a similarly small inner core size, with satellite observations showing a diameter as small as 28 km (Chang and Wong, 2008). The eye of Typhoon *Dolphin* was estimated to be as small as 16 km in diameter during the early stages of rapid intensification (from the IBTrACS dataset). A propensity of low-latitude tropical cyclones to be smaller in inner core size was found in idealized numerical model simulations by DeMaria and Pickle (1988).

In a recent article, Steenkamp *et al.* (2019) examined the evolution of four low-latitude genesis events, including Typhoon *Vamei* (2001), Typhoon *Dolphin* (2015), Tropical Depression (TD) 9C and Hurricane *Pali* (2016), based on European Centre for Medium-Range Weather Forecasts (ECMWF) analyses. They found that the genesis of tropical cyclones near the Equator is no different from genesis at higher latitudes. Provided that there is some large-scale background rotation that encompasses a region of predominantly positive absolute vertical vorticity, deep

convection is able to stretch the background rotation, producing localized regions of enhanced vertical vorticity. Vorticity is concentrated by the overturning circulation produced by the deep convection, which fluxes vertical vorticity towards the centre of the convective region in the lower troposphere. By Stokes' theorem, an increase in vertical vorticity inside a fixed loop leads to an increase in the circulation around the loop.

At this stage, it is worth remarking that there is no generally accepted definition of “genesis” in the literature. As the IBTrACS dataset is a compilation of worldwide best tracks, genesis depends on the issuing agency. For example, the National Oceanic and Atmospheric Administration (NOAA) and Joint Typhoon Warning Center (JTWC) document systems in the best-track data that reach the threshold for a tropical depression (containing central deep convection and a closed Earth-relative low-level centre), even if they do not reach 17 m s^{-1} . In the idealized simulations by Kilroy *et al.* (2017a; 2017b; 2018) and Steenkamp *et al.* (2019), genesis was considered to have occurred at the end of a gestation period in which the maximum azimuthally-averaged tangential wind speed, V_{max} , increased only slowly and when this wind speed began a sharp increase. Typical values of V_{max} at this so-called “tipping point” were a little below the 17 m s^{-1} threshold. We use the same definition for genesis in this study, that is, the time of the sharp increase in intensification rate.

Steenkamp *et al.* (2019) showed that, in the case of Typhoon *Vamei*, a large region of enhanced background relative vorticity formed due to large-scale interactions between a northeasterly monsoon cold surge and an unusually westward-displaced Borneo vortex, an event described by Chang *et al.* (2003) as a one in a hundred year event. In the case of Typhoon *Dolphin*, the large-scale circulation was linked to an unstable roll-up of cyclonic vorticity in a shear line, which marked an intertropical convergence zone. In contrast, both TD² 9C and Hurricane *Pali* formed within a monsoonal shear line that was located on the Equator. In the foregoing cases, the ambient strip of counterclockwise vorticity rolls up into localized gyre pouch circulations. These gyre pouches become the centre

¹During this time period, there are no recorded cases of genesis within 5° of the Equator in the Atlantic Ocean. The first event occurring within 5° of the Equator is recorded in the year 1859 in the South Indian Ocean. There are no data for the maritime continent (where the majority of low-latitude events occur) until 1884.

²It should be pointed out that there is ambiguity in the definition of a Tropical Depression. TD 9C appears to have been classified when its intensity (as defined earlier) was just 7.5 m s^{-1} (from the IBTrACS dataset). The glossary on the NOAA Hurricane Research Division website uses “tropical cyclone” as “the generic term for a non-frontal synoptic-scale low-pressure system over tropical or subtropical waters with organized convection (that is, thunderstorm activity) and a definite cyclonic surface wind circulation”. Notably, this definition does not invoke any wind threshold. The same glossary defines a “tropical depression” as a tropical cyclone with maximum sustained surface winds of less than 17 m s^{-1} (34 kt, 39 mph), that is, with no formal wind threshold on intensity.

of action for the convective vorticity organization process, in accord with the marsupial paradigm of Dunkerton *et al.* (2009).

Typhoon *Vamei* has been the subject of several numerical modeling studies, but, to our knowledge, there have been no such studies of the genesis or intensification of Hurricane *Pali* and Typhoon *Dolphin*. Using the fifth-generation Pennsylvania State University–National Center for Atmospheric Research Mesoscale Model (MM5), Chambers and Li (2007) found that, in a simulation of *Vamei*, mesoscale convective vortices (MCVs) formed along a horizontal shear line on the eastern edge of an “exceptionally strong” monsoonal cold surge, and the vorticity produced by these MCVs subsequently merged to form the core of pre-*Vamei*. For the rapid intensification phase, these authors conducted a vorticity budget which showed that enhanced horizontal fluxes of vorticity toward the storm centre played a major role in spinning up the vortex. In another study of Typhoon *Vamei* using MM5, Juneng *et al.* (2007) highlighted the important role of latent heat fluxes from the surface in both the genesis and rapid intensification phases of the storm, a result that is to be expected.

This present study aims to provide a basic understanding of the genesis and intensification processes of tropical cyclones in the absence of background rotation. To this end, we present in more detail the three idealized numerical simulations that were described only briefly in Steenkamp *et al.* (2019). These simulations are a repeat of the three idealized numerical simulations of Kilroy and Smith (2017) (hereafter KS17), but with the Coriolis parameter set to zero. In Steenkamp *et al.* (2019), the zero Coriolis experiments were presented as evidence that vortex development can occur on the Equator in numerical models, although the focus in that study was on the evolution of observed cases as seen in the ECMWF analyses.

KS17 investigated the effects of initial vortex size on tropical cyclogenesis and intensification remote from the Equator. In their study, the Coriolis parameter, f , was taken to be $2.53 \times 10^{-5} \text{ s}^{-1}$, corresponding to a latitude of 10°N . They found that, as the initial vortex size is increased, cyclogenesis occurs later. Moreover, the size of the vorticity monopole, the sizes of the inner and outer core tangential wind circulations, and the lifetime intensity of the vortex all increase as the initial vortex size is increased. Here, we investigate whether these findings of KS17 hold when f is set to zero and explore in more depth why, in this case, such vortices decay after a few days.

The remaining article is organized as follows. In section 2 we introduce the numerical model used in this study and describe the experimental setup. In section 3 we describe the results of three idealized numerical simulations of tropical cyclogenesis in the absence of the Coriolis

force. In section 4 we describe two additional sensitivity experiments. The conclusions are presented in section 5.

2 | NUMERICAL MODEL AND SIMULATIONS

As in KS17, the numerical simulations are performed using the state-of-the-art CM1 model (version 16), which is a nonhydrostatic and fully compressible cloud model (Bryan and Fritsch, 2002). The model configuration is identical to that in KS17, except that the Coriolis parameter is set equal to zero. In brief, the overall domain is $3000 \times 3000 \text{ km}^2$ in size and contains a central region $300 \times 300 \text{ km}^2$ in size, in which there is a uniform grid spacing of 500 m. Outside this high-resolution inner core, the grid spacing is stretched gradually from 500 m to 10 km near the outer boundary. There are 40 vertical levels from the surface to the domain top at a height of 25 km. The vertical grid spacing stretches smoothly from 50 m at the surface to 1.2 km at the domain top. The Kessler warm-rain microphysics scheme is used for simplicity. In this scheme, raindrops have a fixed fall speed of 7 m s^{-1} . Radiative effects are represented crudely by a simple Newtonian cooling with the default timescale of 12 hr capped at 2 K per day.

The subgrid turbulence scheme used is the model option *iturb=3*, a parametrized turbulence scheme (Bryan and Rotunno, 2009). The horizontal and vertical advection schemes are fifth-order and contain implicit diffusion. A Rayleigh damping layer is applied above a height of 20 km and within 100 km of the lateral boundaries, which, because of the relatively short integration times, are taken to be rigid walls.

The reference sounding is the same as that used in Kilroy *et al.* (2017a): see their figure 1. As described in that article, it is an arithmetic mean of 39 dropsonde soundings obtained on September 12, 2010, during the Pre-Depression Investigation of Cloud Systems in the Tropics (PREDICT) field campaign for the tropical wave-pouch disturbance that later became Hurricane *Karl* (see Montgomery *et al.*, 2012; Smith and Montgomery, 2012 for details). The sea-surface temperature (SST) is 29°C , typical of the Caribbean region at this time of year. Retaining the PREDICT sounding and SST facilitates a direct comparison of the simulations with those of KS17, but one might inquire whether this is realistic for simulations at the Equator. It has been shown that tropical cyclone simulations are quantitatively sensitive to the chosen combination of ambient sounding and SST (see, e.g., Črnivec and Smith, 2017, section 6; Kilroy *et al.*, 2017a, section 5). In particular, the timing of the intensification phase and/or the rate of intensification may be affected. However, the qualitative behavior of vortex evolution is much

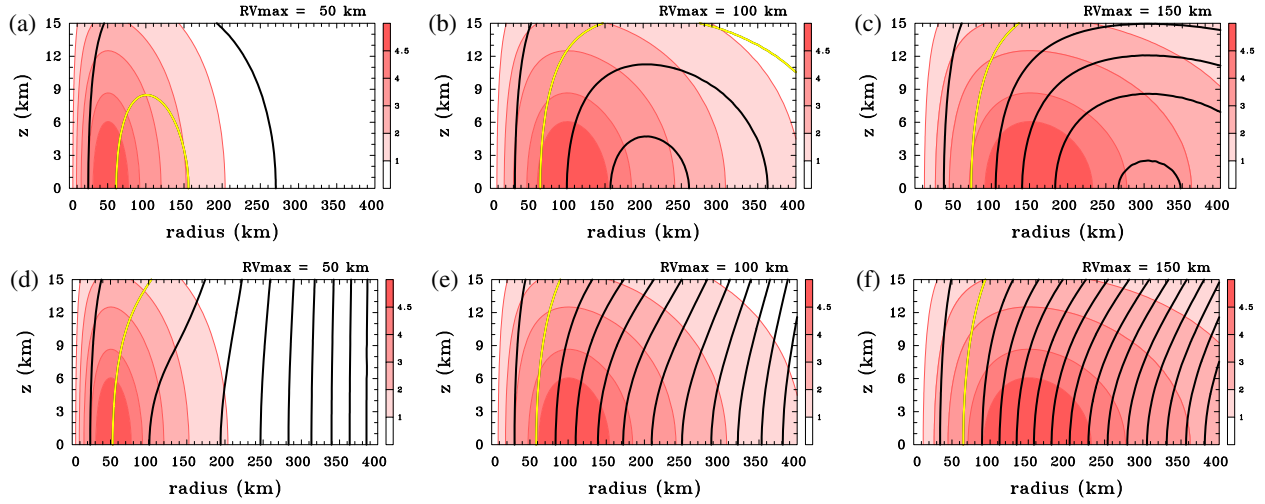


FIGURE 1 Vertical cross-section of the initial tangential wind and absolute angular momentum structure in (a) E1nof, (b) E2nof, and (c) E3nof. Panels (d)–(f) show the equivalent cross-sections of absolute angular momentum for vortices located at 10°N ((d) E1f, (e) E2f, and (f) E3f). Contour intervals: tangential wind as given by the shading in the label bar on the right in m s^{-1} . Black contours of angular momentum every $2 \times 10^5 \text{ m}^2 \text{ s}^{-1}$, starting at $1 \times 10^5 \text{ m}^2 \text{ s}^{-1}$. The $3 \times 10^5 \text{ m}^2 \text{ s}^{-1}$ contour is highlighted in yellow

the same, involving the concentration of absolute vorticity in the lower troposphere by the overturning circulation caused by deep cumulus convection in the inner region of the vortex (see, e.g., Montgomery and Smith, 2017, section 4.1). Thus, we would argue that the observed data from the PREDICT experiment are adequate for the present study.

The three new simulations E1nof, E2nof, and E3nof are the same as those described in KS17, referred to here as E1f, E2f, and E3f, respectively, except that $f = 0$ instead of the value for 10°N . In E1nof and E1f, the initial axisymmetric vortex has a radius of maximum winds located at 50 km, in E2nof and E2f it is located at 100 km, and in E3nof and E3f it is located at 150 km. In each case, the maximum tangential wind speed is 5 m s^{-1} and it is located at the surface. A justification for using a surface-based vortex is given by Steenkamp *et al.* (2019), who showed that, in the four real cases analyzed, development occurred first at low levels. Nevertheless, we have carried out an additional sensitivity experiment with a vortex with an initial midlevel maximum that is described briefly in section 4. The initial vortices are warm-cored and initially cloud-free with no secondary circulation. However, the warm core is extremely weak, with a maximum temperature difference of only 0.1 K located at a height of 15 km on the vortex axis.

The initial tangential velocity profiles are given by the formula

$$v(r) = v_1 s \exp(-\alpha_1 s) + v_2 s \exp(-\alpha_2 s), \quad (1)$$

where $s = r/r_m$ and r_m , v_1 , v_2 , α_1 , and α_2 are constants, so that $v = v_m = 5 \text{ m s}^{-1}$ at $r = r_m = 50, 100,$ and 150 km for Experiments 1, 2, and 3, respectively. The values of v_1 and

α_1 are given by

$$\alpha_1 = (1 - \mu \alpha_2 \exp(-\alpha_2)) / (1 - \mu \exp(-\alpha_2)),$$

$$v_1 = v_m \exp(\alpha_1) (1 - \mu \exp(\alpha_2)),$$

where $\mu = v_2/v_m = 1.0$ and $\alpha_2 = 0.9$. These vortices have essentially zero circulation at large radii, so that, by Stokes' theorem, the cyclonic vorticity of the inner core is surrounded by anticyclonic vorticity at large radii. They have also the desirable feature of finite, spatially integrated kinetic energy and angular momentum.

The three initial tangential velocity profiles are shown in Figure 1a–c, together with the corresponding absolute angular momentum (M) fields.³ In each case, the tangential wind speed decreases sinusoidally with height, becoming zero at a height of 20 km. For comparison, we show in Figure 1d–f the corresponding profiles for the vortices at 10°N , where there are, of course, significant differences in the profiles of angular momentum.⁴ As the vortex size increases, the angular momentum surfaces are spaced more closely together. In cases with $f = 0$, there is a negative radial gradient of m beyond 100 km in E1nof, 205 km in E2nof, and 305 km in E3nof. In contrast, there is a positive radial gradient of M throughout the

³We will hereafter refer to the relative component of angular momentum as angular momentum, or m . In the cases analyzed at the Equator there is no planetary contribution, so that $m = rv$, where r is the radius from the axis, and v is the tangential wind.

⁴The contour interval of M here is different from that given for similar panels shown in figure 1 of KS17. There is actually an error in the M contour interval in KS17. It should be the same as given in the caption to Figure 1 here.

domain in the experiments where f corresponds to 10°N . Regions of negative radial gradient of M satisfy the necessary and sufficient condition for axisymmetric inertial (centrifugal) instability. In the next section, an instability arising in the region satisfying this condition appears to play a prominent role in the demise of emergent tropical cyclones at the Equator.

3 | RESULTS

In the following subsection, we provide a broadscale overview of metrics describing vortex evolution in the three idealized numerical simulations with zero Coriolis parameter, comparing them with the three simulations of KS17 in which the Coriolis parameter is that for 10°N . Then, in section 3.2, we present a comparison of the evolution from an azimuthally-averaged perspective.

3.1 | Overview of evolution

Figure 2 shows time series of the azimuthally-averaged maximum tangential wind speed (V_{\max}), the radius at which this maximum occurs ($R_{v\max}$), and the radius of gale force winds (R_{gales}), defined as the outermost radius of the 17 m s^{-1} tangential wind at a height of 1 km. Both V_{\max} and $R_{v\max}$ can occur at any height, but are found typically well within the boundary layer (less than 1 km height). The left panels show the evolution of the three idealized numerical simulations with zero Coriolis parameter, while for comparison the right panels show the evolution of the three idealized numerical simulations at 10°N taken from KS17.

The evolution of the V_{\max} curves is almost identical for all six experiments until about 36 hr. At this time, the vortices in both E1nof and E1f (Figure 2a,b) undergo a period of rapid intensification (RI). About 12 hr later, the vortices in both E2nof and E2f begin to intensify rapidly, while those in both E3nof and E3f take another 12 hr before they begin to intensify. In other words, the onset of RI occurs at essentially the same time for same-sized initial vortices located at the Equator and at 10°N , indicating that *the Earth's rotation at a latitude of 10°N is not an important factor in the genesis process*, that is, the period leading up to the development of tropical storm strength winds (17 m s^{-1}). In contrast, the Earth's rotation does become more important in vortex evolution after RI begins.

In E1nof, the vortex intensifies for only about 12 hr and then undergoes a mature phase with a quasi-steady V_{\max} for another 12 hr. Thereafter the vortex decays, with a final V_{\max} of 10.8 m s^{-1} at 108 hr. This vortex attains a lifetime maximum V_{\max} of 43.2 m s^{-1} during its short-lived mature phase, while the vortex in E1f reaches a maximum

intensity of 67.5 m s^{-1} . In E1f the vortex is still intensifying at 108 hr.

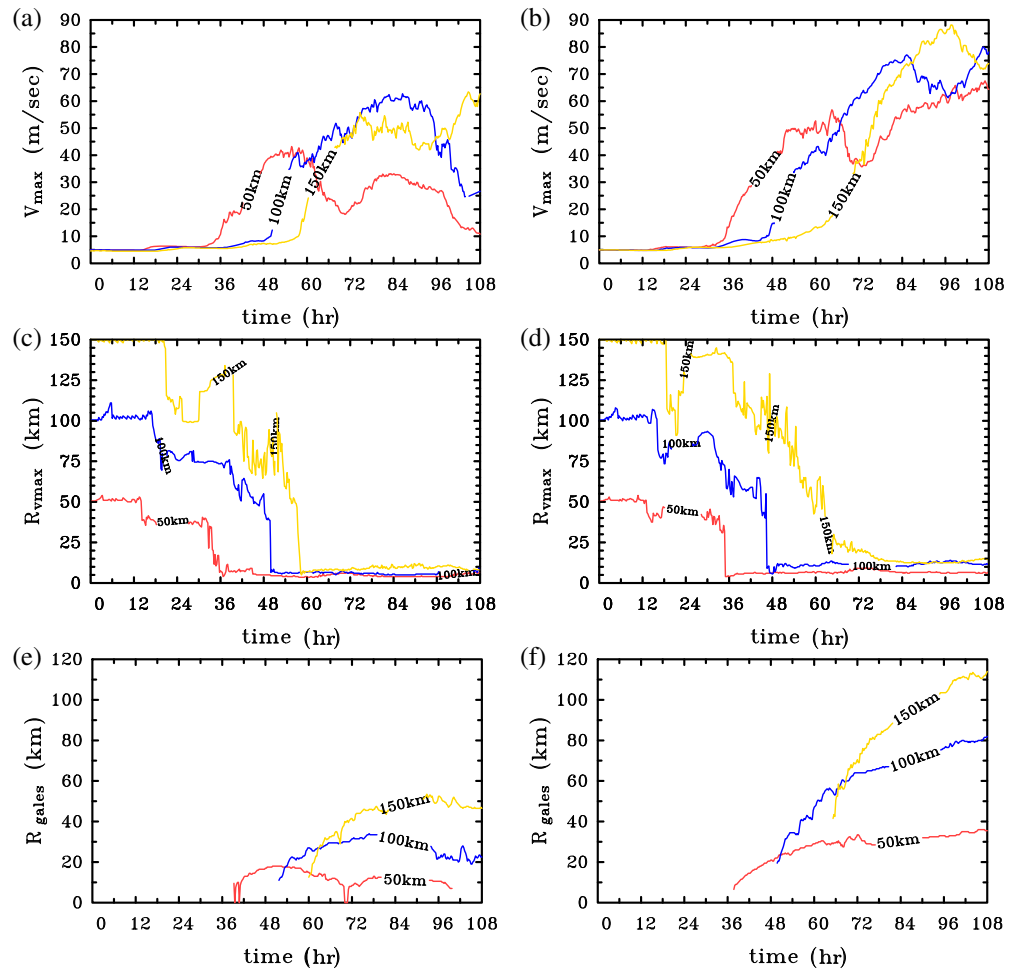
The vortex in E2nof has slightly longer intensification and mature phases than those in E1nof, but decays also within the 108 hr shown here. Again, the vortex at 10°N (E2f) is still intensifying at the end of the simulation. The lifetime maximum V_{\max} is 62.7 m s^{-1} in E2nof, compared with 80.0 m s^{-1} when the vortex is located at 10°N (E2f). In E3nof, the vortex is still intensifying at 108 hr. As will become apparent later, this longer lived vortex is due to the larger initial source of cyclonic angular momentum associated with the broader initial vortex. In E3nof, the lifetime maximum V_{\max} is 63.4 m s^{-1} , compared with 88.2 m s^{-1} when the vortex is located at 10°N (E3f).

As noted in the Introduction, tropical cyclones in both nature and numerical model simulations tend to be smaller in size when they are located closer to the Equator. In the idealized simulations performed here, the inner core size, as characterized by $R_{v\max}$, is larger for all cases at 10°N (Figure 2c,d). For all cases at the Equator, $R_{v\max}$ is less than 10 km at most times following the onset of RI. $R_{v\max}$ in E2nof is typically between 5 and 7 km throughout the mature phase, while in E3nof $R_{v\max}$ is typically between 7.5 and 10 km, although it rises as high as 12 km on occasion. In E2f, $R_{v\max}$ is generally larger than 10 km, while in E3f $R_{v\max}$ is a minimum of 12 km at 90 hr, before rising gradually to about 15 km at 108 hr. All of the storms simulated here have a relatively small mature inner core size. These small mature sizes may be, in part, a result of the relatively small initial vortex sizes. Exploration of this issue is beyond the scope of the present study.

There are large differences also in the outer core size when comparing both sets of experiments. The outer core size of all three vortices at the Equator, R_{gales} (Figure 2d,e), is much smaller than in the cases at 10°N . In particular, after a brief outer core expansion during the mature phase, the outer core decreases in size in all three cases at the Equator, while it is still increasing at 108 hr in all cases at 10°N . After the RI phase, R_{gales} is typically twice as large in the cases located at 10°N compared with the cases located at the Equator. It is noteworthy that, even though the vortex in E3nof is still intensifying near the end of the simulation, its outer core size starts to decrease from about 96 hr.

The evolution of deep convection and vorticity (not shown) is broadly similar, during the genesis and early intensification phase, to that in the corresponding experiments at 10°N , which are shown in KS17. There are, of course, differences in detail between corresponding experiments associated with the stochastic nature of deep convection (Nguyen *et al*, 2008). As in all our recent idealized studies of tropical cyclogenesis (Kilroy *et al*, 2017a; 2017b; 2018), deep cumulus convection and the convectively-induced vertical vorticity distribution are

FIGURE 2 Time series of maximum azimuthally-averaged (a,b) tangential wind speed (V_{\max}), (c,d) radius at which V_{\max} occurs ($R_{v\max}$), and (e,f) radius of gale force winds (R_{gales}) at a height of 1 km (the radius of the outermost 17 m s^{-1} tangential wind) in the idealized numerical simulations with (a,c,e) zero Coriolis parameter and (b,d,f) Coriolis parameter $f = 2.53 \times 10^{-5} \text{ s}^{-1}$, equivalent to 10°N . Experiments with small initial vortices E1nof and E1f (red curve) are labeled “50 km”, experiments with medium-sized initial vortices E2nof and E2f (blue curve) are labeled “100 km”, and experiments with large initial vortices E3nof and E3f (yellow curve) are labeled “150 km”



highly nonaxisymmetric, especially before and during much of the early RI phase. As a result, the emerging vorticity monopole retains a degree of relatively strong asymmetry during this stage. Nevertheless, as in these earlier studies, it proves insightful to investigate vortex development from an azimuthally-averaged perspective, which is the topic of the next section.

3.2 | An azimuthally-averaged view of vortex evolution

Figures 3 and 4 show vertical cross-sections of the azimuthally-averaged, 3-hr time-averaged tangential $\langle v \rangle$, radial $\langle u \rangle$ and vertical $\langle w \rangle$ velocity components at 36 and 60 hr in E1nof (panels a,b), at 48 and 72 hr in E2nof (panels c,d), and at 54 and 78 hr in E3nof (panels e,f). Also shown are contours of time and azimuthally-averaged angular momentum $\langle m \rangle$. The time averaging is centered on the given times. In each simulation, the former time is just before the intensification start time and the latter time is 24 hr later, during the RI phase. Here we focus on the three new simulations at

the Equator. The corresponding simulations at 10°N are analysed in detail in KS17.

The onset of the RI phase occurs at about 36 hr in E1nof (Figure 2a). At this time, deep convection has focused near the vortex axis (Figures 3a and 4a), with the largest values of $\langle w \rangle$ occurring between heights of about 5 and 10 km. There are regions of subsidence in the lowest 2 km between radii of 20 and 50 km. The subsidence is associated with the cooling from evaporation of rainfall in addition to the drag on the air exerted by the rain. The maximum $\langle v \rangle$ at this time is just over 10 m s^{-1} and the radius of this maximum is less than 20 km. There is weak inflow in the lower troposphere, below about 7 km, with outflow above this height. The inflow is a maximum at the surface within a radius of 10 km. At this stage, the structure of $\langle m \rangle$ is somewhat similar to that at the initial time, except at low levels, where the $\langle m \rangle$ surfaces have a large vertical gradient on account of the loss of $\langle m \rangle$ due to friction at the surface.

Just 24 hr later, at 60 hr (Figure 3b), there have been dramatic changes in vortex structure. Deep convection is now much stronger, as characterized by larger values of $\langle w \rangle$, and it is confined largely within a radius of

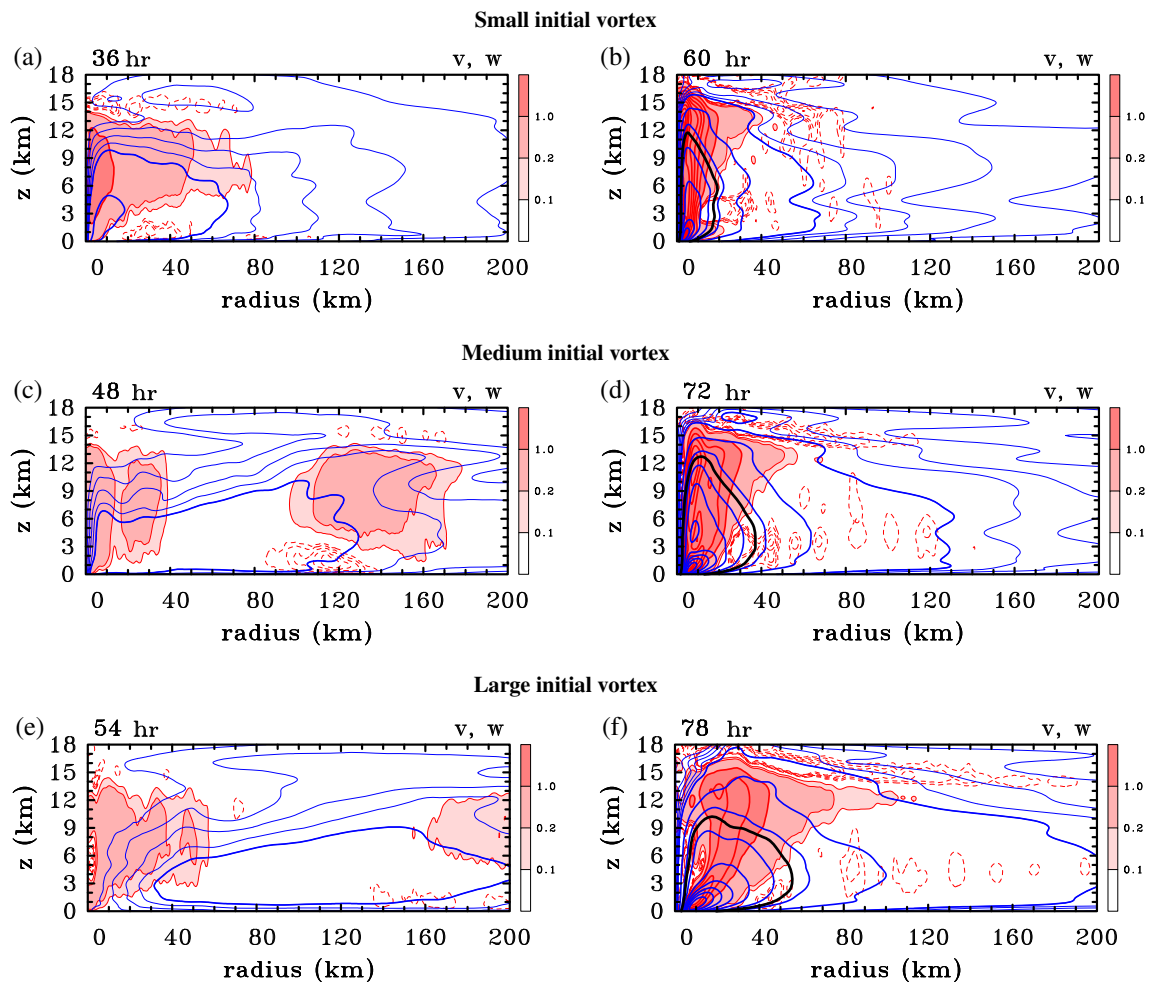


FIGURE 3 Vertical cross-sections of the azimuthally-averaged, 3-hr time-averaged vertical and tangential velocity components centered on the time shown in E1nof (top panels), E2nof (middle panels), and E3nof (bottom panels). Contour intervals are as follows. Tangential velocity: thin blue contours 1 m s^{-1} between 1 and 4 m s^{-1} , thick blue contours every 5 m s^{-1} , thick black contour 17 m s^{-1} . Vertical velocity shading as indicated on the side bar in m s^{-1} . Positive vertical velocity is contoured (solid contours) every 1 m s^{-1} in the region of darkest shading. Negative vertical velocity is contoured (dashed contours) every 0.02 m s^{-1} from -0.02 to -0.1 m s^{-1}

20 km from the axis. The vortex has strengthened considerably, with a maximum $\langle v \rangle$ of nearly 40 m s^{-1} at this time. This maximum occurs at low levels within the strong inflow layer. There is now a shallow and relatively strong boundary-layer inflow with two alternating layers of outflow and inflow above, extending radially to over 130 km. These two layers of radial flow above the boundary layer are not present in the analogous case at 10°N (see section 3.3 below). Since, in the absence of appreciable eddy effects, $\langle m \rangle$ is approximately materially conserved by the azimuthally-averaged transverse circulation, these layers of radial flow act to modify the structure of $\langle m \rangle$. Now there are two distinct regions enclosed by the yellow $\langle m \rangle$ contour (the $3 \times 10^5 \text{ m}^2 \text{ s}^{-1}$ contour). During the next 6-hr period, the vortex in E1nof decays rapidly (Figure 2a). The reasons for this decay are examined in sections 3.3 and 3.4.

For E2nof (Figures 3c,d and 4c,d), we show first the vortex structure at 48 hr, just before the RI phase begins (panel c). At this time there is a broad region with $\langle v \rangle$ greater than 5 m s^{-1} out to a radius of 120 km, and the location of maximum $\langle v \rangle$ has reduced to about 60 km (Figure 2c). There are three distinct regions of deep convective ascent ($> 1 \text{ m s}^{-1}$): one centered on the axis, another centered at a radius of about 25 km, and a broad region centered at a radius of about 130 km (Figure 3c). There is a pronounced region of subsidence beneath the outermost region.

There is a shallow layer of weak inflow near the surface at small radii, extending to at least 60 km, with outflow near the surface from a radius of about 110 km (Figure 4c). Significantly, the change from inflow to outflow lies beneath the region of strong subsidence. The $\langle m \rangle$ surfaces have a “nose” at a height of 3 km, which

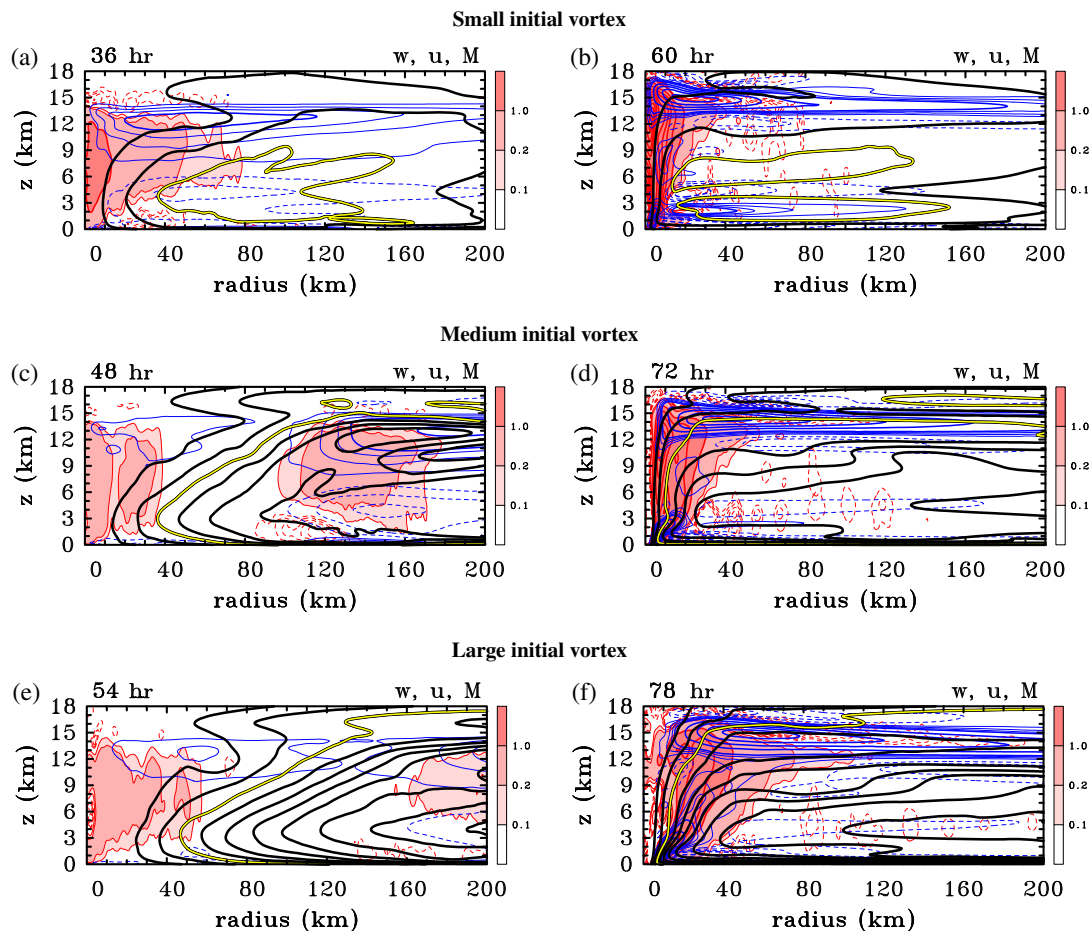


FIGURE 4 Vertical cross-sections of the azimuthally-averaged, 3-hr time-averaged vertical and radial velocity components and angular momentum in E1nof (top panels), E2nof (middle panels), and E3nof (bottom panels). Contour intervals are as follows. Radial velocity: thin blue contours 1 m s^{-1} between 1 and 3 m s^{-1} , thick blue contours every 4 m s^{-1} . Dashed contours negative, positive contours solid. Vertical velocity shading as indicated on the side bar. Positive vertical velocity is contoured (solid contours) every 1 m s^{-1} in the region of darkest shading. Negative vertical velocity is contoured (dashed contours) every 0.02 m s^{-1} from -0.02 to -0.1 m s^{-1} . Contours of angular momentum every $1 \times 10^5 \text{ m}^2 \text{ s}^{-1}$, with the $3 \times 10^5 \text{ m}^2 \text{ s}^{-1}$ contour highlighted in yellow

coincides with the level of strongest inflow at this time. The maximum inflow is just over 3 m s^{-1} at a radius of about 150 km .

At 72 hr (Figures 3d and 4d), the vortex has strengthened considerably, the maximum $\langle v \rangle$ being close to 50 m s^{-1} at a radius of just under 10 km , and again within the strong inflow layer. There is now a second tangential wind maximum at a height of about 4.5 km in the eyewall updraught. This maximum is part of a developing centrifugal wave initiated by the layer of strong outflow just above where the boundary-layer inflow terminates (Persing *et al.*, 2013). This wave is apparent also in the radial velocity field, where it is marked by alternating layers of outflow and inflow in the eyewall. While such a secondary maximum is not seen in composite studies of tropical cyclone structure (e.g., Rogers *et al.*, 2013, figure 3), it is frequently found in individual hurricanes (see, e.g., Stern *et al.*, 2018). The maximum inflow (almost 30 m s^{-1}) now occurs at

the surface and appreciable inflow (exceeding 1 m s^{-1}) is evident out to 200 km radius. The $\langle m \rangle$ surfaces have moved a considerable distance inwards since 48 hr . The next 24 hr are characterized by a quasi-steady mature phase, beyond which the vortex rapidly decays (Figure 2a).

In E3nof, the vortex development is similar to that in the other cases: first deep convection focuses near the axis and RI follows shortly afterwards. At 54 hr , there has been little amplification of the vortex (Figure 3e) and the mean secondary circulation is most apparent in the weak outflow in the upper troposphere (Figure 4e). As in the earlier cases, the $\langle m \rangle$ surfaces have a pronounced nose in the lower troposphere.

Just 24 hr later, the maximum $\langle v \rangle$ has increased to nearly 50 m s^{-1} and occurs now at a radius of about 10 km and a height of a few hundred metres (Figure 3f). In this case, the eyewall updraught is weaker, but covers a larger area than those in E1nof and E2nof. Moreover, it has a

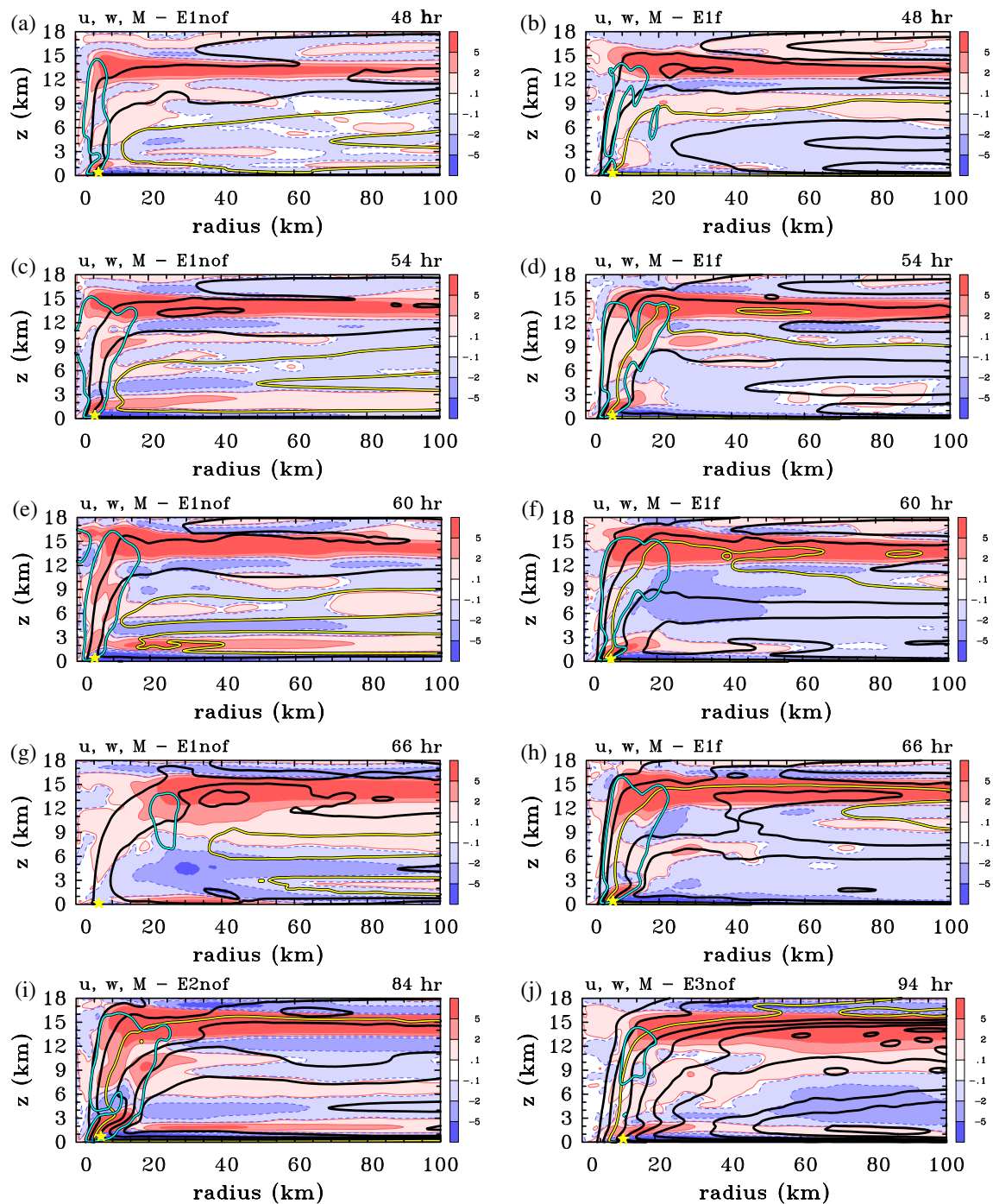


FIGURE 5 Vertical cross-sections of the azimuthally-averaged vertical and radial velocity components and angular momentum in Elnof (panels a,c,e,g) and in Elf (panels b,d,f,h) at 6-hr intervals from 48–66 hr. The lower panels show E2nof at 84 hr and E3nof at 94 hr. Contour intervals are as follows. Vertical velocity: aqua contour 2 m s^{-1} . Radial velocity shading as indicated on the side bar in m s^{-1} . Contours of absolute angular momentum every $1 \times 10^5 \text{ m}^2 \text{ s}^{-1}$, with the $3 \times 10^5 \text{ m}^2 \text{ s}^{-1}$ contour highlighted in yellow. The location of v_{max} is highlighted by a yellow star symbol

noticeably larger outward tilt. In other respects, the pattern of secondary circulation is similar to that shown in the other cases, with strong boundary-layer inflow, feeding the eyewall updraught and a layer of strong outflow in the upper troposphere (Figure 4f).

3.3 | Onset of inertial/centrifugal instability

While the main purpose of this article is to investigate tropical cyclogenesis at the Equator, it is of interest to

examine briefly the reasons for the rather rapid decay seen in E1nof and E2nof. It turns out that the seeds of the decay process emerge during the mature stage and to highlight these we focus first on E1nof. Figure 5 shows a selection of radius–height cross-sections of the azimuthally-averaged radial flow and m surfaces for this simulation. These cross-sections are not time-averaged. These fields are compared with similar ones from E1f (showing M surfaces) at the same times. Figure 5a,b compares the fields at 48 hr, about the time when the vortex in E1nof has reached its peak intensity. At this time, there are still many similarities between the two simulations. Both show a shallow near-surface layer of strong inflow inside a radius of 40 km, both show a shallow layer of strong outflow near the radius where the boundary-layer inflow terminates, and both show a layer of strong outflow in the upper troposphere. However, whereas in E1f there is mostly inflow in the lower half of the troposphere beyond a radius of about 20 km, in E1nof there are shallow layers of alternating inflow and outflow in this region.

By 54 hr (Figure 5c,d), the layered pattern of inflow and outflow in E1nof has become more pronounced as the radial flow has increased in strength in these layers. Moreover, the layer of outflow immediately above the shallow boundary-layer inflow has extended out to beyond 100 km. In contrast, in the E1f simulation, the outflow that emerges as air ascends out of the boundary layer terminates just beyond 20 km radius and there is a deep layer of inflow out to at least 45 km. Beyond that radius, there is a layer of weak outflow in the lower troposphere, but animations of the fields show this to be a short-lived feature, which, during the hour that follows, disappears altogether (not shown).

At 60 hr, which marks the beginning of the decay phase in E1nof, the layered pattern of inflow and outflow is apparent throughout the troposphere (Figure 5e), whereas in E1f, there is generally inflow between heights of 3 and 12 km (Figure 5f). The outflow layer just above the boundary layer in E1f does extend to a larger radius (about 60 km) than at 54 hr, but again, outflow at this level occurs in pulses, presumably related to the ability of deep convection to ventilate the mass that is converging in the boundary layer at a particular time (Kilroy *et al.*, 2016).

At 66 hr, the flow pattern in E1nof (Figure 5g) has changed dramatically from that 6 hr earlier (Figure 5e). The eyewall updraught has completely decayed, but an upper-level feature of this convection remains at radii between about 20 and 30 km. Significantly, there is now outflow throughout the boundary layer from a radius of 10 km to about 70 km. The m surfaces have moved outwards significantly, which is a feature of the spin down of the vortex over this time period. In contrast, the vortex in E1f (Figure 5h) continues to intensify, with inflow

occurring from a radius of 20 km and beyond to a height of about 6 km.

Similar layered structures develop during the mature phase in E2nof and E3nof, but they take longer to form when the initial vortex is larger. This behavior is illustrated in Figure 5i,j, which shows the vortex structure for E2nof at 84 hr and for E3nof at 94 hr. At these times, both vortices have tongues of outflow above the boundary layer that extend out to at least 100 km. There is no analogous behavior in E2f or E3f (not shown). Subsequently, outflow develops down to the surface and the vortices spin down rapidly. This development begins in the inner core at about 102 hr in E2nof, and at about 96 hr in E3nof, although it occurs at larger radii (outside 100 km) in this simulation (not shown).

The layered pattern of inflow and outflow in these simulations at the Equator seen in Figure 5 does not fit with known paradigms for tropical cyclone behavior. However, it is reminiscent of the layered nature of Taylor instability for flow between concentric cylinders in which the inner cylinder is rotating and the outer cylinder is at rest (Taylor, 1923). This idealized flow is one of the simplest manifestations of inertial instability. At the Equator, realistic counterclockwise vortices with finite kinetic energy and therefore zero circulation at large radii must be surrounded by a region of clockwise vertical vorticity in which, at the Equator, the flow would be centrifugally unstable. Figure 6 shows the extent of these centrifugally unstable regions in all three simulations during the mature phase. It is significant that the early development of layered inflow and outflow structures occurs in these unstable regions. The shallow nature of the layers in the simulations presented here is presumably related to the relatively strong stable stratification of the flow.

3.4 | The decay process

The low-level outflow in E1nof seen in Figure 5g heralds the beginning of a rapid decay phase (Figure 1a). Deep convection is initiated along the inner boundary of this outflow and propagates outwards with time. This convection is highlighted in Figure 7, which shows horizontal cross-sections of the vertical component of relative vorticity and wind vectors at a height of 1 km at 60 and 66 hr, as well as the 2 m s^{-1} contour of vertical velocity at a height of 6 km. At 60 hr, the flow is relatively symmetric, with a central core of deep convection encompassing a monopole of strong ($> 2 \times 10^{-3} \text{ s}^{-1}$) vertical vorticity. There is a broad field of anticyclonic vorticity just outside the core at this time, with two distinct regions of strong ($< -0.5 \times 10^{-3} \text{ s}^{-1}$) anticyclonic vorticity occurring on the edge of the convective region. At 66 hr (Figure 7b), the

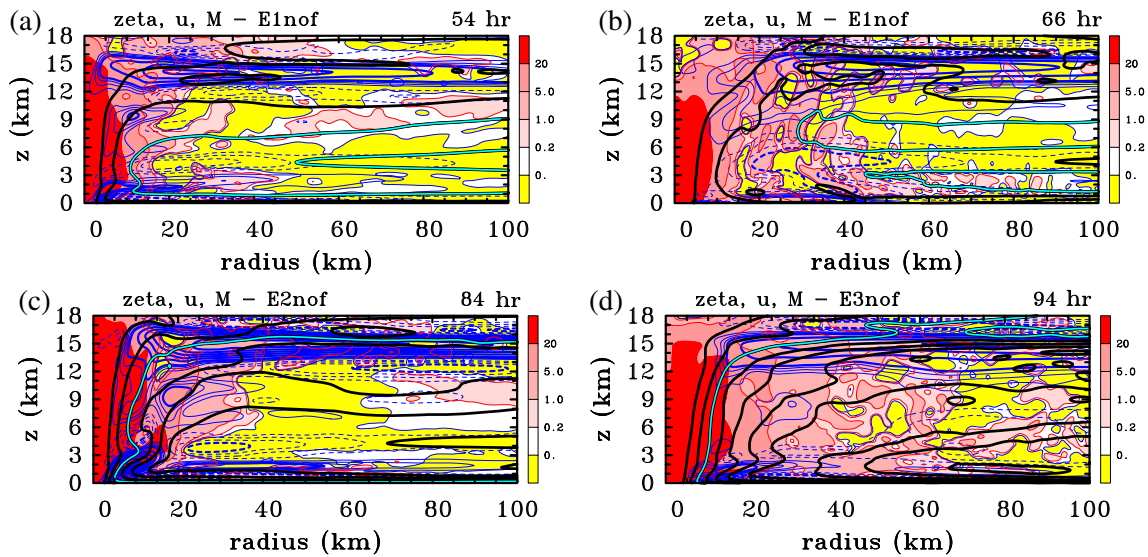


FIGURE 6 Vertical cross-sections of the azimuthally-averaged vertical vorticity, radial velocity and angular momentum in (a,b) E1nof, (c) E2nof, and (d) E3nof at selected times. Vertical vorticity shading as indicated on the side bar, multiplied by 10^{-4} s^{-1} . Contour intervals are as follows. Radial velocity: thin blue contours every 1 m s^{-1} from 1 to 3 m s^{-1} . Thick blue contours every 4 m s^{-1} . Contours of angular momentum every $1 \times 10^5 \text{ m}^2 \text{ s}^{-1}$, with the $3 \times 10^5 \text{ m}^2 \text{ s}^{-1}$ contour highlighted in aqua. Yellow shading shows regions of negative relative vorticity

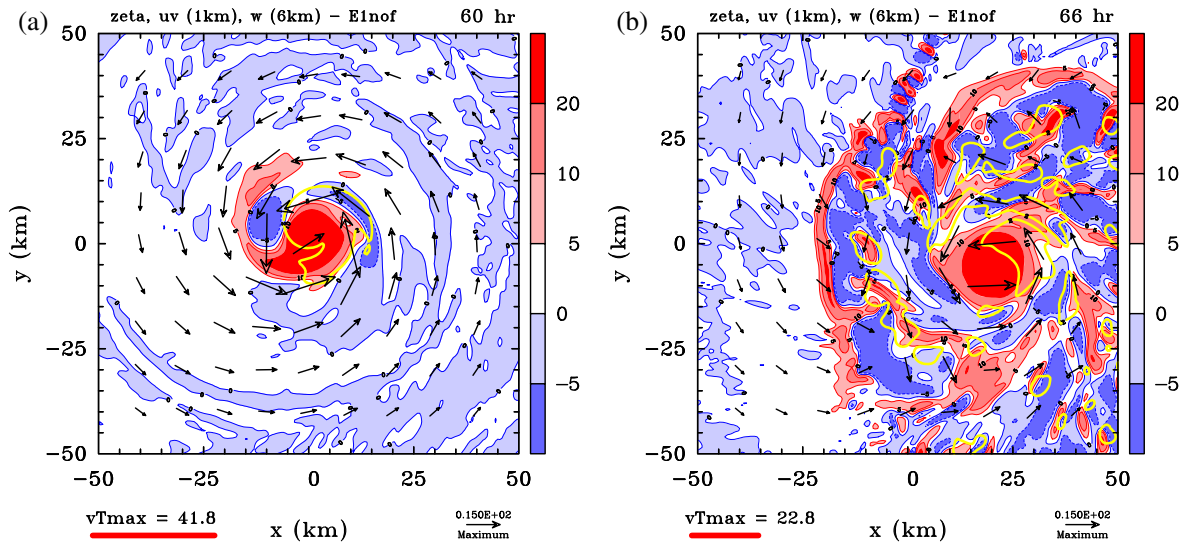


FIGURE 7 Horizontal cross-sections of the vertical component of relative vorticity and the wind vectors at (a) 60 hr and (b) 66 hr at 1 km altitude. Also shown are contours of vertical velocity at a height of 6 km (yellow). Values for the shading of vertical vorticity are given in the color bar, multiplied by 10^{-4} . The yellow vertical velocity contour is 2 m s^{-1} . The wind vectors are in relation to the maximum reference vector at the bottom right, while on the bottom left the maximum total wind speed in the domain plotted is given in m s^{-1}

fields have changed dramatically, with the flow becoming highly asymmetric. The convective core has broken down and deep convection covers much of the domain shown. Animations of the fields show that the dipole band of positive and negative vorticity is propagating outwards at this time and is colocated with a band of strong ascent at a height of 1 km.

To investigate further the development of outflow near the ocean surface in E1nof at 66 hr seen in Figure 5g

and the initiation of deep convection that accompanies it, we show in Figure 8 vertical cross-sections of the azimuthally-averaged radial and vertical flow in the lowest 5 km at 2 hr intervals leading up to and beyond this time. Also shown are the $\langle m \rangle$ contours. These fields are not time-averaged. We focus here on E1nof only, as the decay occurs in this simulation earlier than in the other two $f = 0$ simulations, although the behavior is similar in those simulations at later times (not shown).

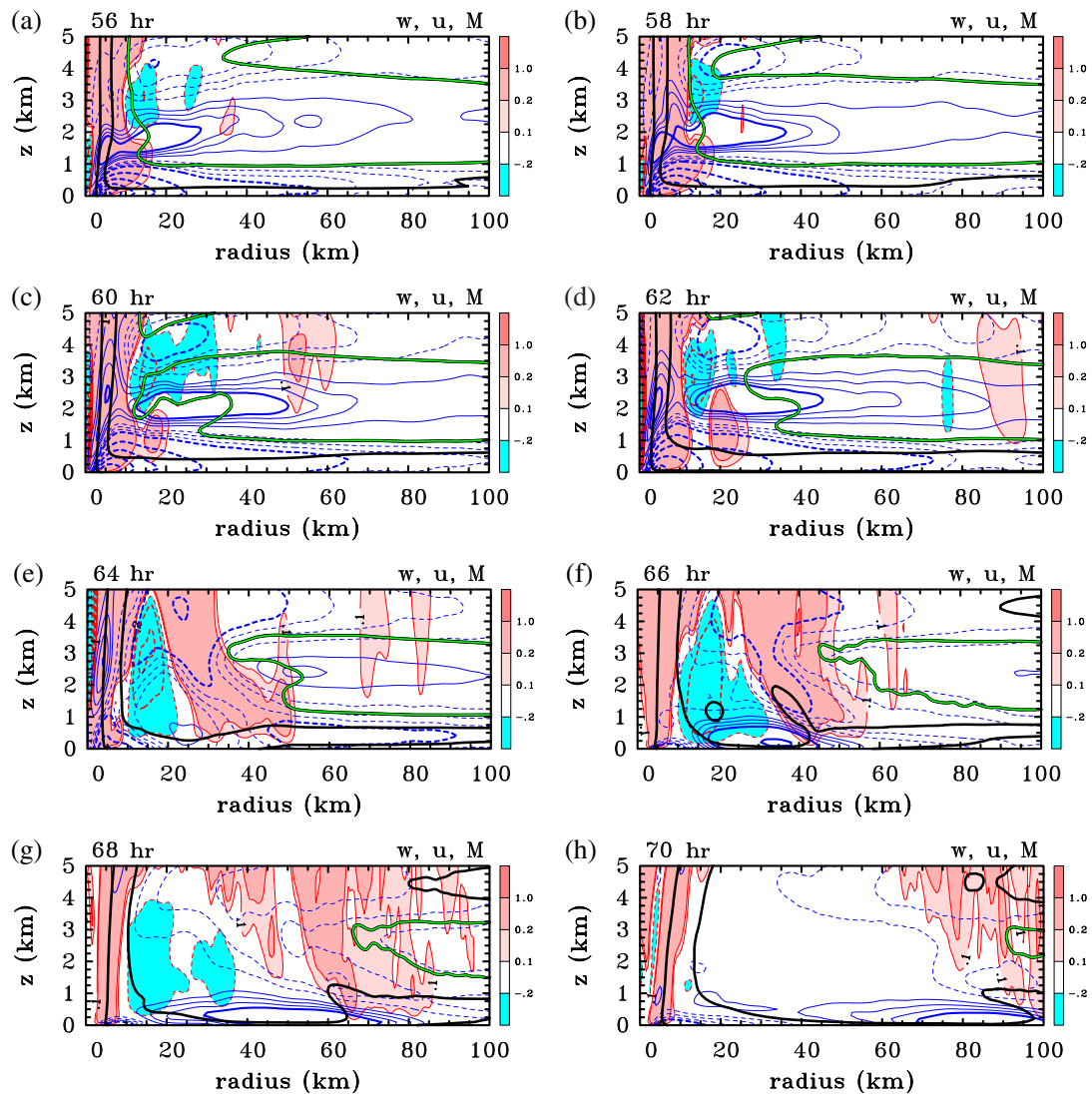


FIGURE 8 Vertical cross-sections of the azimuthally-averaged vertical and radial velocity components and angular momentum in Elnof at 2 hr intervals starting at 56 hr. Contour intervals are as follows. Radial velocity: thin blue contours 1 m s^{-1} between 1 and 3 m s^{-1} , thick blue contours every 4 m s^{-1} . Vertical velocity shading as indicated on the side bar in m s^{-1} . Contours of angular momentum every $1 \times 10^5 \text{ m}^2 \text{ s}^{-1}$, with the $3 \times 10^5 \text{ m}^2 \text{ s}^{-1}$ contour highlighted in green

At 56 hr (Figure 8a), there is relatively strong frictionally induced boundary-layer inflow extending to a radius of at least 100 km, with upflow restricted to the central core of convection. Above the boundary layer, there is already a relatively strong outflow region centered at a height of about 1.5 km, with another inflow layer above that centered at a height of about 4 km. There is some relatively strong subsidence at this time between heights of 2 and 4 km at a radius of 15 km. During the following 4 hr (Figure 8b,c), the region of strong ($< -0.2 \text{ m s}^{-1}$) subsidence increases in strength and expands radially outwards. At the same time, the upper inflow increases in strength.

Between 60 and 62 hr (Figure 8c,d), the subsidence increases in strength and extends below a height of 2 km.

The core convection appears to split into two distinct regions. Following this split, strong subsidence develops between the two updraught regions and extends into the boundary layer at 64 hr (Figure 8e). At this time, the outflow between 2 and 3 km height decays, while the strong inflow above increases in strength and in areal extent. Further, the boundary layer inflow has been interrupted and there is now a spatially localized region of outflow developing near the surface at a radius of 25 km. This outflow strengthens and increases in areal coverage in the next 2 hr (Figure 8f), while the subsidence strengthens further in the boundary layer. From 68 hr (Figure 8g), the surface outflow region spreads outwards, while the vertical motion in the domain shown (both up and down-draughts) weakens. There is now mainly ascent at larger

radii in a region of convergence (at about 80 km), where the inflow and outflow regions meet at the surface. This ascent is linked to a band of deep convection (Figure 7b), which moves outward along the leading edge of the outflow. At 70 hr, V_{\max} is substantially weaker than 12 hr earlier (Figure 1).

The strengthening outward jet of air between heights of about 1.5 and 3 km, and the inward jet directly above that, would appear to be a result of the presence of inertial instability. It is hard to unravel the interaction between the evolving layered structure of inflow and outflow and deep convection, which must be tightly coupled components of the overall flow. It would appear that the subsidence into the boundary layer is an element of this layered structure near the rotation axis. Presumably, the deep convection near the axis is unable to ventilate all of the radial mass flux in the elevated layer of inflow associated with this instability.

The realism of these simulations beyond the time where inertial instability occurs is hard to judge, based on the meagre observational data that are available. Only one of the five cases of near-Equatorial cyclogenesis investigated by Steenkamp *et al.* (2019) showed a region of negative relative vorticity within about 2° – 3° of the storm centre. That was the case of Typhoon *Vamei* in late December (see Steenkamp *et al.*, 2019, figure 3). In this regard, *Vamei* would have been more closely equivalent to the large vortex studied here. However, small tropical cyclones may be easily missed in areas with sparse observations (J. Courtney 2019, personal communication). Because of the uncertainty in its realism, we are reluctant to investigate further the behavior of the vortex decay stage in the foregoing simulations.

4 | SENSITIVITY EXPERIMENTS

In this section, we present briefly two sensitivity experiments that were suggested by reviewers of an earlier draft of the article. The first is a repeat of the E2nof simulation, but with a vortex that has an initial midlevel maximum tangential wind speed instead of a surface-based one. The initial vortex structure for this new simulation is shown in Figure 9a. The initial vortex has a maximum tangential wind speed of 5 m s^{-1} located at a height of 5.5 km and at a radius of 100 km. The initial wind speed maximum at the surface is just under 2 m s^{-1} .

Figure 9b shows the evolution of the tangential wind speed maximum for the vortex in this simulation. The vortex starts to intensify rapidly at about 60 hr, compared with an intensification start time of 48 hr for the vortex with a surface-based maximum located at the same radius. The vortex is weaker and shorter-lived than its

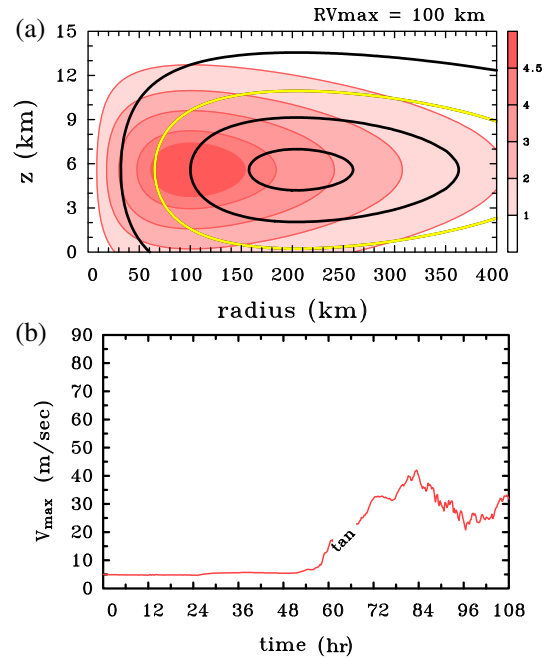


FIGURE 9 (a) Vertical cross-section of the initial tangential wind and relative angular momentum structure in the equatorial midlevel vortex case. Contour intervals: tangential wind as given by the shading in the label bar on the right in m s^{-1} . Black contours of angular momentum every $2 \times 10^5 \text{ m}^2 \text{ s}^{-1}$, starting at $1 \times 10^5 \text{ m}^2 \text{ s}^{-1}$. The $3 \times 10^5 \text{ m}^2 \text{ s}^{-1}$ contour is highlighted in yellow. Panel (b) shows a time series of maximum azimuthally-averaged tangential wind speed (V_{\max}) for this simulation

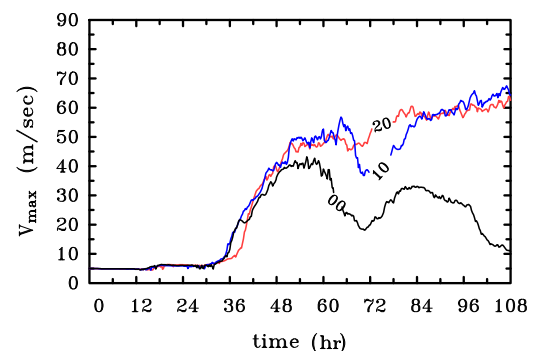


FIGURE 10 Time series of maximum azimuthally-averaged tangential wind speed (V_{\max}) for the E1nof case (labeled “00”), the E1f case (labeled “10”), and the case at 20°N (labeled “20”)

surface-based equivalent, with a lifetime V_{\max} of 40 m s^{-1} compared with 62.7 m s^{-1} in the surface-based case. Presumably the vortex is weaker because the initial vortex has lower values of cyclonic relative vorticity at and near the surface. The development of the midlevel vortex is very similar to the case with the surface-based vortex, in that, once deep convection becomes prevalent near the centre of the circulation, the low levels begin to spin up rapidly. Similar breakdown events linked to inertial instability (as discussed in section 3) occur at later times also (not shown).

The second sensitivity experiment is a repeat of E1f, but with the Coriolis parameter set to a value equivalent to 20°N instead of 10°N. The evolution of V_{\max} for this simulation, and for the two other small initial vortex cases (E1f and E1nof), is shown in Figure 10. The onset time of RI is roughly the same in all three cases, with that in the 10°N case occurring slightly before the equatorial case, and that in the 20°N case occurring about 2 hr later. The vortex at 20°N does not undergo any periods of decay during the time period shown here, unlike the vortices in E1f and E1nof.⁵ Given the stochastic nature of deep convection, one would expect some small differences in the onset times. This result suggests further that the Coriolis parameter does not play an important role in the genesis process, at least in the cases of small initial vortices.

5 | CONCLUSIONS

We have investigated the formation of idealized tropical cyclones at the Equator using a state-of-the-art numerical model, starting from a prescribed weak (maximum wind speed 5 m s⁻¹) initial vortex in an otherwise quiescent, nonrotating environment comprising the mean thermodynamic structure of a recent genesis field experiment. We carried out three main simulations with the Coriolis parameter set to zero and compared the vortex evolution with that in a previous study where the Coriolis parameter has a value equivalent to 10°N. In the three simulations, the radius of maximum tangential wind speed is set to 50, 100, or 150 km, as in the previous study.

In each case, both at the Equator and at a latitude of 10°N, the vortex developed rapidly after a gestation period of between 30 and 60 hr. The evolution during this gestation period is essentially the same at the Equator as at 10°N. After a relatively short mature phase, the vortices on the Equator decay as the initial core of cyclonic vorticity is depleted. As in the case of vortices away from the Equator, the larger the initial vortex, the longer the gestation period, the stronger the lifetime maximum tangential wind speed,

and the larger the mature inner and outer core sizes. A new finding is that the larger the initial vortex, the longer the mature phase at the Equator.

The vortex evolution during the decay phase is quite dissimilar to that in simulations away from the Equator. As the vortex matures, layered structures of inflow and outflow develop throughout the troposphere, beginning first in the lower troposphere. These layered structures are presumably a result of inertial/centrifugal instability that develops as the region of instability in the outer part of the vortex is drawn inwards by the convectively driven overturning circulation. They are reminiscent of the Taylor–Couette rolls that arise in the centrifugally unstable flow between concentric cylinders when the inner cylinder rotates and the outer one is at rest, but they are shallow, on account of the relatively strong stable stratification in the atmosphere. Vortex decay in the simulations appears to be intimately related to the development of this instability, but the decay process does not correspond to known paradigms for tropical cyclone behavior.

Centrifugally unstable regions surrounding vortices may certainly develop in nature, as clockwise vorticity of Southern Hemisphere origin is wrapped around a counterclockwise vortical circulation centered at or near the Equator, or as counterclockwise vorticity of Northern Hemispheric origin is wrapped around a clockwise vortical circulation centered at or near the Equator. Therefore, the vortex evolution described here during the mature stage may have some degree of realism. However, without guidance from observations, a detailed investigation of the decay phase would seem unwarranted at this time.


In summary, the results of this study support the hypothesis that tropical cyclogenesis on the equator, where $f = 0$, is possible in principle provided there is a sufficient reservoir of relative vorticity initially to concentrate. Development continues for some time until the reservoir is exhausted and a decay phase ensues dominated by centrifugal instability.

ACKNOWLEDGEMENTS

We are grateful to Kerry Emanuel and two anonymous reviewers for their thoughtful and thorough reviews of the original manuscript. We thank George Bryan for generously making his model available to the community. GK acknowledges financial support for tropical cyclone research from the German Research Council (Deutsche Forschungsgemeinschaft) under Grant number KO 2248/2-1. MTM acknowledges the support of NSF grants AGS-1313948 and IAA-1656075, ONR grant N0001417WX00336, and the U.S. Naval Postgraduate School. The views expressed herein are those of the authors and do not represent sponsoring agencies or institutions.

⁵From a V_{\max} perspective, the period of weakening in E1f starting at around 66 hr looks similar to the decay period in E1nof, which starts at 60 hr, but the vortex structure is very different in the inner core region during the times of decay in these simulations (not shown). It appears that a small localized region of inertial instability develops in the inner core region in the case at 10°N. This region of instability coincides with a short-lived tongue of outflow at the top of the boundary layer. However, both the outflow tongue and region of inertial instability decay quickly at 10°N, and do not occur at all at 20°N. Only on the Equator is there persistent development of a vertically layered inflow–outflow structure, and only on the Equator does outflow develop along the surface. At the Equator there are widespread regions of inertial instability throughout the depth of the troposphere.

ORCID

Gerard Kilroy  <https://orcid.org/0000-0002-9240-6555>
 Roger K. Smith  <https://orcid.org/0000-0002-3668-1608>
 Michael T. Montgomery  <https://orcid.org/0000-0001-5383-4648>

REFERENCES

- Anthes, R.S. (1982) *Tropical Cyclones: Their Evolution, Structure and Effects*, (p. 208). Boston, MA: American Meteorological Society.
- Bryan, G.H. and Fritsch, J.M. (2002) A benchmark simulation for moist nonhydrostatic numerical models. *Monthly Weather Review*, 130, 2917–2928
- Bryan, G.H. and Rotunno, R. (2009) The maximum intensity of tropical cyclones in axisymmetric numerical model simulations. *Monthly Weather Review*, 137, 1170–1179
- Chambers, C. and Li, T. (2007) Simulation of formation of a near-equatorial typhoon Vamei (2001). *Meteorology and Atmospheric Physics*, 98, 67. <https://doi.org/10.1007/s00703-006-0229-0>
- Chang, C.P., Liu, C.H. and Kuo, H.C. (2003) Typhoon Vamei: an equatorial tropical cyclone formation. *Geophysical Research Letters*, 30, 1150. <https://doi.org/10.1029/2002GL016365>, 3.
- Chang, C.P. and Wong, T.S. (2008). Rare typhoon development near the Equator. In K.N. Liou, M.D. Chou, and H.H. Hsu (Eds.), *Recent Progress in Atmospheric Sciences: Applications to the Asia-Pacific Region*, pp. 172–181: World Scientific.
- Črnivec, N. and Smith, R.K. (2017) Mean radiosonde soundings for the Australian monsoon/cyclone season. *International Journal of Climatology*, 37, 66–78
- DeMaria, M. and Pickle, J.D. (1988) A simplified system of equations for simulation of tropical cyclones. *Journal of the Atmospheric Sciences*, 45, 1542–1554
- Dunkerton, T.J., Montgomery, M.T. and Wang, Z. (2009) Tropical cyclogenesis in a tropical wave critical layer easterly waves. *Atmospheric Chemistry and Physics*, 9, 5587–5646
- Fortner, L.E. (1958) Typhoon Sarah, 1956. *Bulletin of the American Meteorological Society*, 39, 633–639
- Gill, A.E. (1982) *Atmosphere–Ocean Dynamics* Vol. 1982, p. 662). London: Academic Press.
- Holliday, C.R. and Thompson, A.H. (1986) An unusual near-equatorial typhoon. *Monthly Weather Review*, 114, 2674–2677
- Houze, R.A. (1993) *Cloud Dynamics*, (p. 570). San Diego, CA: Academic Press.
- Juneng, L., Tangang, F. and Reason, C. (2007) Simulation of tropical cyclone Vamei (2001) using the PSU/NCAR MM5 model. *Meteorology and Atmospheric Physics*, 97, 273. <https://doi.org/10.1007/s00703-007-0259-2>
- Kilroy, G., Montgomery, M.T. and Smith, R.K. (2017a) The role of boundary-layer friction on tropical cyclogenesis and intensification. *Quarterly Journal of the Royal Meteorological Society*, 143, 2524–2536
- Kilroy, G. and Smith, R.K. (2017) The effects of initial vortex size on tropical cyclogenesis and intensification. *Quarterly Journal of the Royal Meteorological Society*, 143, 2832–2845
- Kilroy, G., Smith, R.K. and Montgomery, M.T. (2016) Why do model tropical cyclones grow progressively in size and decay in intensity after reaching maturity?. *Journal of the Atmospheric Sciences*, 73, 487–503
- Kilroy, G., Smith, R.K. and Montgomery, M.T. (2017a) A unified view of tropical cyclogenesis and intensification. *Quarterly Journal of the Royal Meteorological Society*, 143, 450–462
- Kilroy, G., Smith, R.K. and Montgomery, M.T. (2018) The role of heating and cooling associated with ice processes on tropical cyclogenesis and intensification. *Quarterly Journal of the Royal Meteorological Society*, 144, 99–114
- Knapp, K.R., Kruk, M.C., Levinson, D.H., Diamond, H.J. and Neumann, C.J. (2010) The international best track archive for climate stewardship (IBTrACS): unifying tropical cyclone best track data. *Bulletin of the American Meteorological Society*, 91, 363–376
- Montgomery, M.T., Davis, C., Dunkerton, T., Wang, Z., Velden, C., Torn, R., Majumdar, S.J., Zhang, F., Smith, R.K., Bosart, L., Bell, M.M., Haase, J.S., Heymsfield, A., Jensen, J., Campos, T. and Boothe, M.A. (2012) The pre-depression investigation of cloud systems in the tropics (PREDICT) experiment: scientific basis, new analysis tools and some first results. *Bulletin of the American Meteorological Society*, 93, 153–172
- Montgomery, M.T. and Smith, R.K. (2017) Recent developments in the fluid dynamics of tropical cyclones. *Annual Review of Fluid Mechanics*, 49, 541–574
- Nguyen, S.V., Smith, R.K. and Montgomery, M.T. (2008) Tropical-cyclone intensification and predictability in three dimensions. *Quarterly Journal of the Royal Meteorological Society*, 134, 563–582
- Persing, J., Montgomery, M.T., McWilliams, J. and Smith, R.K. (2013) Asymmetric and axisymmetric dynamics of tropical cyclones. *Atmospheric Chemistry and Physics*, 13, 12249–12341
- Pielke, R.A. and Pielke, R.A. (1997) *Hurricanes: Their Nature and Impacts on Society*, (p. 279). New York, NY: John Wiley & Sons.
- Rogers, R.F., Reasor, P. and Lorsolo, S. (2013) Airborne doppler observations of the inner-core structural differences between intensifying and steady-state tropical cyclones. *Monthly Weather Review*, 141, 2970–2991
- Smith, R.K. and Montgomery, M.T. (2012) Observations of the convective environment in developing and non-developing tropical disturbances. *Quarterly Journal of the Royal Meteorological Society*, 138, 1721–1739
- Steenkamp, S.C., Kilroy, G. and Smith, R.K. (2019) Tropical cyclogenesis at and near the Equator. *Quarterly Journal of the Royal Meteorological Society*, 1–19. <https://doi.org/10.1002/qj.3529>
- Stern, D.P., Kepert, J.D., Doyle, J.D. and Bryan, G.H. (2018). Understanding atypical midlevel wind speed maxima in hurricane eyewalls. In: 33rd Conference on Hurricanes and Tropical Meteorology. Jacksonville, FL: Amer. Meteorol. Soc., 8C.6 .
- Taylor, G.I. (1923) Stability of a viscous liquid contained between two rotating cylinders. *Proceedings of the Royal Society London. A*, 223, 605–615
- Wallace, J.M. and Hobbs, P.V. (2006) *Atmospheric Science Second Edition: An Introductory Survey*, (p. 483). Amsterdam, the Netherlands: Academic Press/Elsevier.

How to cite this article: Kilroy G, Smith RK, Montgomery MT. An idealized numerical study of tropical cyclogenesis and evolution at the Equator. *Q.J.R. Meteorol. Soc.* 2019;1–16. <https://doi.org/10.1002/qj.3701>